The final publication is available at

https://doi.org/10.1088/1748-0221/12/12/C12018

Additional Information

A scintillator geometry suitable for very small PET gantries

Antonio J. Gonzalez[1], Andrea Gonzalez-Montoro, Albert Aguilar, Gabriel Cañizares, Rosana Martí, Sofia Iranzo, Efthimis Lamprou, Sebastian Sanchez, Filomeno Sanchez, and Jose M. Benlloch

Instituto de Instrumentación para Imagen Molecular (I3M), Centro Mixto CSIC — Universitat Politècnica de València, Camino de Vera s/n, 46022 Valencia, SPAIN
E-mail: agonzalez@i3m.upv.es

ABSTRACT: In this work we are describing a novel approach to the scintillator crystal configuration as used in nuclear medicine imaging. Our design is related to the coupling in one PET module of the two separate crystal configurations used so far there: monolithic and crystal arrays. The particular design we have studied is based on a two-layer scintillator approach (hybrid) composed of a monolithic LYSO crystal (5-6 mm thickness) and a LYSO crystal array with 4-5 mm height (0.8 and 1 mm pixels). We show here the detector block performance, in terms of spatial, energy and DOI information, to be used as a module in the design of PET scanners. The design we propose allows one to achieve accurate three-dimensional spatial resolution (including DOI information) while assuring high detection efficiency at reasonable cost. Moreover, the proposed design improves the spatial response uniformity across the whole detector module, and especially at the edge region. The crystal arrays are mounted in the front and were well resolved. The monolithic crystal inserted between crystal array and the photosensor, provided measured FWHM resolution as good as 1.5-1.7 mm including the 1 mm source size. The monolithic block achieved a DOI resolution (FWHM) nearing 3 mm. We compared these results with an approach in which we use a single monolithic block with total volume equals to the hybrid approach. In general, comparable performances were obtained.

KEYWORDS: Positron Emission Tomography; Monolithic crystals; Crystal arrays; Silicon Photomultiplier.

---

[1] Corresponding author.

Table of contents

1. Introduction

With the increasing number of animal models of human diseases, e.g., transgenic mice, Positron Emission Tomography (PET) represents an essential non-invasive tool to assess physiological functions in small animal studies [1][2][3][4][5]. It is necessary to visualize and accurately measure radiopharmaceutical accumulation in structures that have dimensions down to a millimeter or even less. This requires the detector to achieve both high spatial resolution and sensitivity. Recently, there is also very high interest in the development of PET/MRI systems capable of simultaneous acquisition of Magnetic Resonance Imaging (MRI) and PET images [6][7][8][9]. True PET/MRI integration requires PET detectors that are very compact, do not distort the operation of the MRI system and are insensitive to magnetic fields to provide simultaneously PET and MRI images. Silicon photomultipliers (SiPM) are being used in the development of current generations of PET/MRI systems due to their compactness, insensitivity to magnetic fields and high signal-to-noise ratio [10].

In this work we describe a novel approach to the scintillator crystal configuration for applications in nuclear medicine imaging. Our design is mainly focused on the implementation of high performance PET detector modules to be used in PET scanners dedicated to imaging human organs or small animals. Our research is specifically related to the coupling of the two crystal configurations that are extensively but separately used so far: monolithic blocks and crystal arrays. Moreover, the proposed detector module design is compatible with MRI scanners. There are advantages and disadvantages of the monolithic and pixelated crystal designs that have been described in the literature [11]. Some advantages of the continuous monolithic crystal design are higher detection sensitivity per unit area (no crystal dead areas), better spatial detection uniformity (no sharp discontinuities), continuous positioning (no pixelation artifacts), depth-of-interaction (DOI) reconstruction capability, and lower cost. Advantages of the pixelated crystal designs are that intrinsic spatial resolution is uniform across the modules, defined primarily by the crystal size, focused scintillation light cone (better signal-to-noise ratio), and in general improved spatial response linearity. Partially slotted crystals [12] have also been considered elsewhere. The partially-optically isolated crystals approach was extensively used in the past, when the pitch of the photodetectors (photomultipliers) was much coarser than that of the discrete scintillation crystals. In that approach, the crystals-pixels are not completely optically isolated and some controlled light sharing across the photodetector plane occurs. Although, this effect can also be produced by simply adding a separate light diffuser between the crystal array and photodetector plane, in this case there is no extra amount of scintillator material, and thus there is no additional increase of sensitivity for the same detector module thickness. This work shows the feasibility of combining monolithic and pixelated

crystal arrays to provide enhanced performance of gamma-ray detectors, especially suited for PET scanner designs.

In the approach we have studied, improving upon our previous pilot research [13], we consider a two-layer scintillator design: a monolithic LYSO crystal layer optically coupled to a pixelated LYSO array. The main goal of the design we propose is to achieve high three-dimensional spatial resolution (including DOI information) while assuring high detection efficiency at a reasonable cost. We have studied main hybrid detector performances assuming two small size crystal designs, both with the incoming radiation impinging first on the pixelated scintillation array placed in the front of the module. The photosensor is placed at the bottom of the detector stack with respect to the impinging radiation and reads-out the scintillation light from both components of the hybrid scintillator module. Light from the first outer component of the module is reaching the photodetector by traversing the second inner scintillator piece that operates in this case as the light guide. At the same time the plate scintillator is also functioning as active material detecting additional incoming gamma radiation. The crystal array provides high resolution, whereas the monolithic block helps increasing the system sensitivity. The two blocks still provide high DOI performance.

2. Materials and Methods

2.1 Materials

We have carried out tests with two volumes of scintillation material, 25 mm × 25 mm × 10 mm (case 1) and roughly 25 mm × 16 mm × 10 mm^3 (case 2). Small volumes improve the Noise Equivalent Count Rates (NECR) performance and allow one for more compact designs. All scintillation material is of the type LYSO (Proteus, Ohio, USA). Optical coupling between different elements of the detector package was achieved using optical grease (type BC630, Saint Gobain). The performance obtained with the hybrid approaches has been compared to data obtained with a single monolithic block with dimensions matching the combined (pixelated plus monolithic) hybrid volumes. Figure 1 shows the four studied cases. The monolithic blocks have lateral walls black painted. For cases 1.1 and 2.1, the entrance face was covered with an optical device called retroreflector that bounces back the light to the emission source [14]. In the hybrid approach, the monolithic crystal has a thickness of 5 mm for case 1.2 but 6 mm for case 2.2. The LYSO crystal array had 1 mm size and 5 mm height pixels (case 1.2) and 0.8 mm size and 4 mm height (case 2.2), respectively. All pixels were as-cut (not polished) and covered by reflective material (Enhanced Specular Reflector, ESR, 3M™). The entrance face of the crystal arrays was also covered with ESR film.
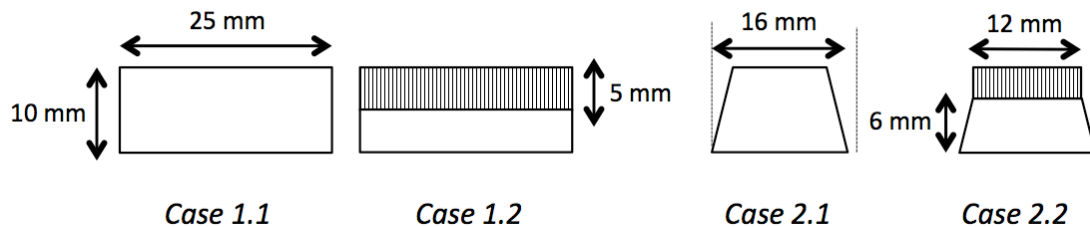

Figure 1. Sketch of the front size for the four crystal cases studied. All have about 25 mm size in the perpendicular direction to the drawing. The line pattern on the top blocks represents the crystal arrays.

We have used SiPM arrays of 16×16 elements (MicroFJ-30035 TSV, SensL, Ireland) that have an active area of $3\times3mm^2$ and a pitch of 3.26 mm. The measurements were carried out at a temperature of about 18±2 ºC. The supplied bias voltage to the SiPM array was 28-29 V. In these experiments, when performed in coincidence, we used a reference detector based on an identical photodetector array (256 SiPMs) with a monolithic crystal with dimensions of $50\times50\times10$ mm^3. The readout makes use of a network providing information for each SiPM row and column output [5][6].

2.2 Methods

The signals obtained from the readout electronics were fed to Analog to Digital Converter (ADC) boards with 12 bit precision and 250 ns integration window. A software collimation of 2.4º from the normal has been applied to all data and, selected as a compromise between performance and statistics. The XY planar impact positions are calculated using a center of gravity algorithm of the projected scintillation light distribution through the readout chain. All digitized row and column signals are raised to the power of two before the center of gravity calculation [15]. In the case of the monolithic blocks, the spatial resolution is studied using collimated positron-emitter sources. We have calculated the measured FWHM of the imaged distributions at the photosensor, after calibration into metric units. The measured FWHM depends on the size source, and this has not been subtracted in all presented data.

The readout allows one to also provide information on the photon DOI in the monolithic blocks since the scintillation light distribution is determined. Here, for each detection event, the ratio of the energy and the maximum value for each row and column (E/I) is calculated and the average value obtained [16]. The DOI performance was evaluated by using collimated 511 keV photons beams impinging on the lateral walls of the scintillation blocks. After calibration of the measured data (E/I units) into metric units (mm), we determined the average FWHM of the DOI distributions.

3. Results

3.1 Case 1.1

A ^{22}Na source (0.25 mm in diameter) was mounted in the front of a Tungsten collimator (2 mm drilled hole, 30 mm thick, 60 mm outer diameter) and scanned in steps of 0.5 mm across the surface (1D) of the monolithic block to study both the spatial and energy resolutions. In Figure 2 left we show the measured FWHM for all point impacts. As expected, best results are obtained for impacts in the crystal center due to a reduced light distribution truncation. Figure 2 right depicts the energy resolution as a function of the beam position. As for the spatial resolution, better energy resolution values are also obtained at the crystal center where it is possible to transfer the highest amount of scintillation photons to the photosensor. Average spatial and energy resolutions of 1.6±0.4 mm and 13±1% were found, respectively.

Concerning the performance of the photon depth of interaction, we carried out experiments with the source impinging laterally to the crystal block in steps of 1 mm. An average DOI resolution (FWHM) of 3.1±0.5 mm was obtained for the whole crystal volume.
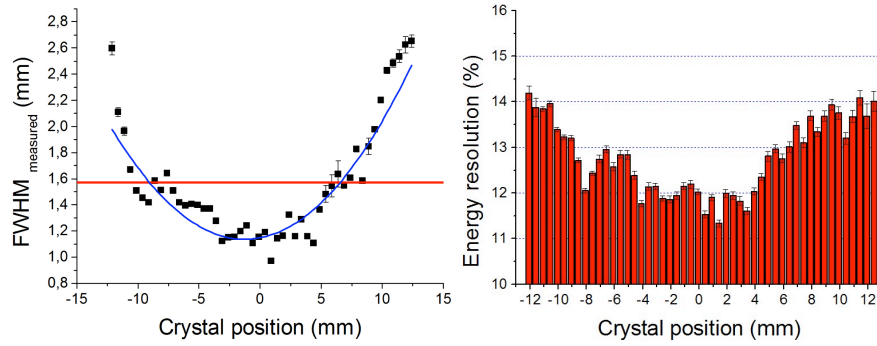
Figure 2. Measured FWHM (left) and energy (right) resolutions, as a function of the beam position in the crystal surface.

3.2 Case 1.2

Case 1.2 includes the hybrid approach of a monolithic and a pixelated block (1 mm pixels) of the same thickness (5 mm). The spatial resolution is differently studied for the two crystal types. For the evaluation of the spatial resolution performance of the crystal array, we used an extended [22]Na source at a distance of 1 cm to the crystal block working in singles mode. Figure 3 left shows the flood map of one acquisition. Both crystal contributions are included in this contour plot. In Figure 3 center we depict the measured energy distribution for a small region of interest (ROI) of about 3×3 LYSO pixels at the detector center. The contribution of the two crystals is very well differentiated, with the one for the crystal array at high ADC channels, whereas impacts in the monolithic block are identified at lower channels. This is understood as more scintillation photons are transferred to the photosensor in the first case. Notice that in the monolithic crystal there is more light spread and, thus, more light absorption in the black walls. The impacts corresponding to the crystal array are isolated by an energy filter of 15% at the photopeak (channels 530-720 in Figure 3 center). We have studied the spatial resolution by measuring the peak-to-valley ratio (P/V). Notice that all pixels were resolved though. We determined a P/V of about 4.3±0.5, see Figure 3 right. The measured energy resolution for single crystal pixels is as good as 8.4%.
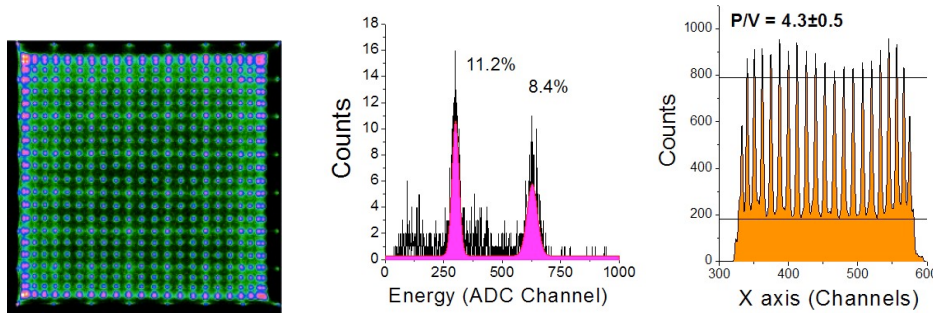

Figure 3. Left, flood map obtained for the hybrid case 1.2. Center, energy spectra for a small ROI. Right, one row of pixels after energy filtering at the photopeak of the pixelated contribution.

The contribution of the two crystal types regarding the DOI is also different. Figure 4 shows the DOI distributions for the two crystal types after energy filtering using normal incidence beams to the crystal. Different from the energy contributions case, the DOI data for the two crystals overlap. The crystal array contribution results in a single thin profile, whereas the DOI distribution for the monolithic follows the expected decay law [14]. Nevertheless, in

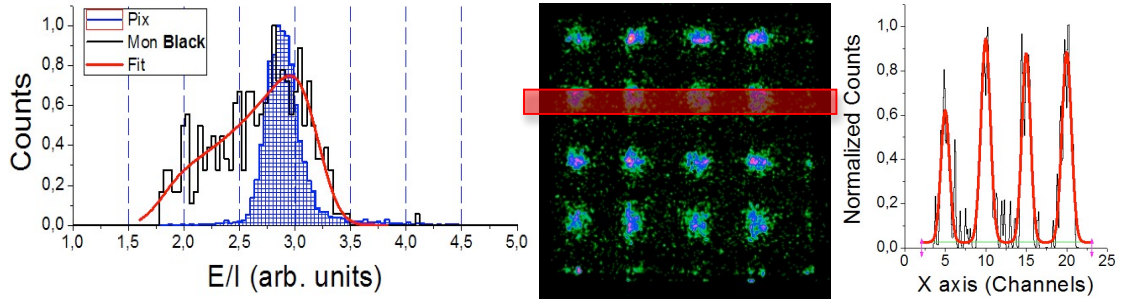this experiment it was sufficient to separate the two crystals contributions by means of the energy filters.

Figure 4. Left, DOI distributions for the pixelated and monolithic blocks (energy filtering). Center, flood map of collimated sources (monolithic contribution). Right, profile for the marked row of sources.

To evaluate the performance of the monolithic crystal, a 5×5 ^{22}Na sources array (1 mm diameter, 5 mm pitch) was placed in front of a collimator (1.2 mm drilled holes, 24 mm thick Tungsten) and a software collimation also applied to the data in order to provide spatial and energy resolution information on the monolithic block. A slightly worse energy resolution was determined for this block, on average 13±1%. Figure 4 center depicts the flood map obtained for the monolithic crystal block, including energy filtering around its photopeak (15%, channels 255-345). The measured spatial resolution is calculated using multi Gaussian fits as depicted in Figure 4 right. We found an average FWHM for all measured sources of 1.6±0.2 mm.
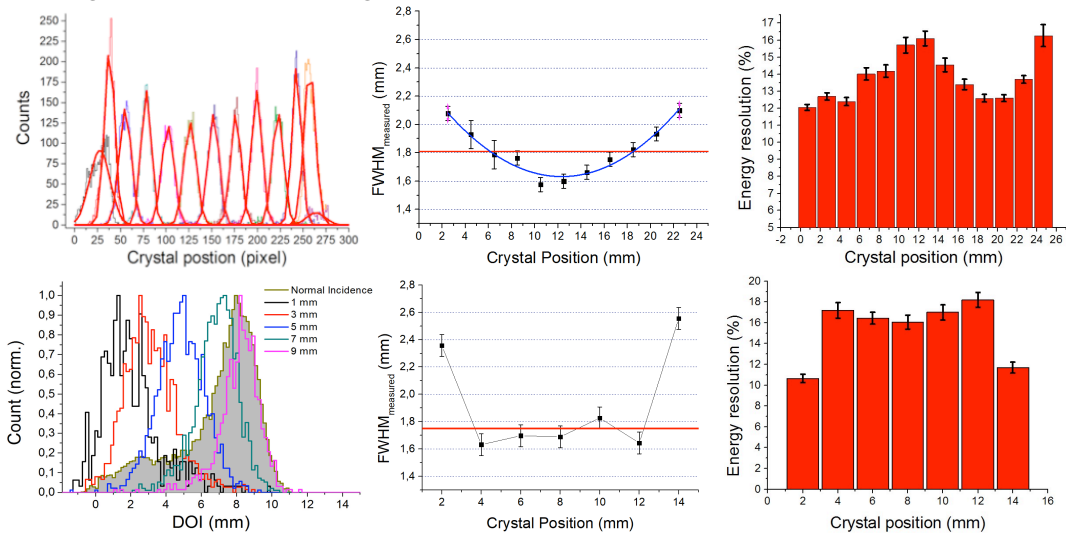

Figure 5. Results for the long (top) and short (bottom) axis. Top-left, profiles of the sources. Top-center, measured FWHM as a function of the impact position. Top-right, energy resolution vs. impact position. Bottom-left, DOI distribution for lateral and perpendicular beams. Bottom-center, measured FWHM as a function of impact position. Bottom-right, energy resolution vs. impact position.

3.3 Case 2.1

The ^{22}Na source and pinhole collimator described in case 1.1 have been used also for case 2.1. Due to the rectangular block shape, the source and collimator were moved across the short and long axial axes of the monolithic crystal. Figure 5 top-left shows the measured profiles for the long axis in pixel channels. The central panel in this figure depicts the measured FWHM.

The energy resolution dependency is also shown on the right hand side. On the bottom panels, center and right, we depict the results for the short axis. Although degradation was observed towards the crystal edges, as expected, both axes resulted on an average measured spatial resolution of 1.8±0.2 mm. The energy resolution was also measured as a function of the impact position, see bar plots in this figure. Again, consistent average energy resolutions were observed for the two axes of about 15±1 %.

The DOI performance is shown in Figure 5 bottom-left. We depict 5 distributions in steps of 2 mm through lateral incidence to the crystal. The plot also shows the DOI profile obtained when radiation impinges normal to the entrance face (grey full curve). We obtained average FWHM values for the DOI of 2.5±0.5 mm.

3.4 Case 2.2

For this case, two crystal pixel sizes were considered (0.8 and 1 mm pitch). As we described for the case 1.2, when the two crystal types are combined we differentiate well the two contributions by the energy spectra. Figure 6 shows on the top-left panel a flood map when uniform radiation is applied. By selecting events in the 15% energy window of the crystal array (see Figure 6 bottom-left), we determined the P/V for both crystal arrays. Figure 6 top-center shows a projection along the long axis for the 1 mm size crystal array. The system showed the capability to resolve all pixels and exhibits a P/V of 3.6±0.8 for the 1 mm pixels and 1.9±0.7 for the 0.8 mm pixels. The spatial resolution for the monolithic contribution is again obtained using the coincidence detector. The collimated ^{22}Na source (0.25 mm) was scanned along the two axes of the hybrid crystal assemble. We obtained similar average results for the two axes (1.6-1.7)±0.5 mm, see Figure 6 top-right.
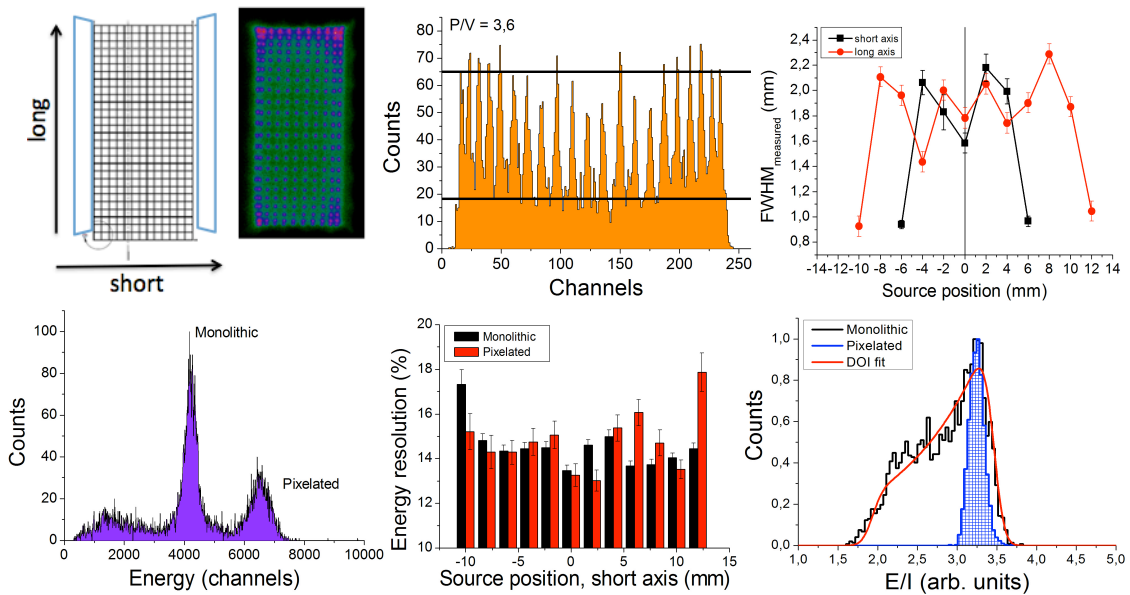

Figure 6. Top-left, sketch and flood map obtained for case 2.2 with 0.8 mm pixels. Center panel shows profile for one row of 1 mm crystal pixels. Top-right, measured FWHM as function of the impact position for the short and long for the monolithic block. Bottom-left, energy distribution for a centered ROI. Bottom-center, measured energy resolution for contributions on the two crystals. Bottom-right, DOI distributions for the two crystal types.

On the bottom of this figure, the energy spectra for a small ROI is shown, where both contributions can be separated, although in this realization the separation of the two photopeaks

is slightly smaller than that observed in case 1.2. The energy resolution was studied after DOI filtering the data, in the ranges of 0-3 and 3.1-4.0 (E/I units) for the monolithic and pixelated cases, respectively (see bottom-right panel in this figure). This figure also shows the energy resolution results for the short axis for the two crystal contributions, finding an average of 15±2%. The data for the long axis also returned similar results of about 14±1%, not shown in the figures.

By using a beam with lateral incidence to the scintillators we observed the different DOI performance for the two crystals. Impacts in the monolithic crystal return DOI values dependent on the beam height, as expected. However, the impacts occurring on the crystal arrays always return the same DOI value. An average DOI resolution of 2.7±0.4 mm was determined for the monolithic block.

4. Discussion and conclusions

A proof of concept for a novel monolithic-pixelated hybrid crystal configuration has been studied. In particular, two crystal volumes have been tested, as described in case 1 and case 2. The current results can be extended to other detector sizes. The proposed design improves the spatial response uniformity across the whole detector module, and especially at the edge regions. It is expected to use the information of the crystal arrays (0.8 and 1 mm size) as a prior information in reconstruction algorithms. This array permits to accurately define a high intrinsic resolution front detector (0.8 mm) while its sensitivity is increased by means of adding the monolithic slab behind it. Since most of the scintillation light in the crystal array is transferred through the continuous scintillator without significant losses, its energy resolution and position resolving power are mostly preserved.

In this work, pixel sizes as small as 0.8×0.8 mm^2 were resolved for this type of scintillator configuration, whereas a detector FWHM spatial resolution of the monolithic block as good as 1.6 mm was obtained (case 2.2). Moreover, the hybrid approach provides different types of DOI information, discrete (4-5 mm) in the case of the crystal arrays but continuous for the monolithic slabs with a DOI FWHM in 2-3 mm range. This would translate into at least 3-4 DOI regions for a 5+5 mm (crystal array + monolithic) total thickness of the hybrid crystal.

The measured energy distributions indicate a differentiation that is good enough to separate both crystal contributions. There are means to further separate the two energy contributions, as for instance using higher light yield pixelated crystals (LFS, GAGG…). In addition to the energy information, DOI characterization also served to distinguish between the two sets of events.

The hybrid concept can be extended to more than two components. For example the pixelated array can be split into two or more arrays. Using staggered configuration with the arrays shifted sideways against each other could potentially provide another means to get better DOI definition.

Acknowledgments

References

[1] R. Myers, *The biological application of small animal PET imaging*, Nucl. Med. Biol. 28, 585–593, 2001.

[2] A. F. Chatziioannou, *Molecular imaging of small animals with dedicated PET tomographs*, Eur. J. Nucl. Med. Mol. Imaging 29, 98–114, 2002.

[3] S. R. Cherry, *Fundamentals of positron emission tomography and applications in preclinical drug development*, J. Clin. Pharmacol. 41, 482–491, 2001.

[4] S.P. Hume and R. Myers, *Dedicated small animal scanners: A new tool for drug development?*, Curr. Pharm. Des. 8, 1497–1511, 2002.

[5] A.J. Gonzalez, A. Aguilar, P. Conde, et al., *A PET Design Based on SiPM and Monolithic LYSO Crystals: Performance Evaluation*, IEEE Trans. Nucl. Sci. 99, 1-7, 2016.

[6] A.J. González, S. Majewski, F. Sánchez, et al., *The MINDView brain PET detector, feasibility study based on SiPM arrays*, Nucl. Instrum. Meth. A 818, 82-90, 2016.

[7] P. Cerello, F. Pennazio, M.G. Bisogni, et al., *An innovative detector concept for hybrid 4D-PET/MRI imaging*, Nucl. Instrum. Meth. A 702, 6–9, 2013.

[8] H. S. Yoon, G. B. Ko, S. Il Kwon, C. Mi Lee, M. Ito, In Chan Song, D. S. Lee, S. J. Hong, J. S. Lee, *Initial Results of Simultaneous PET/MRI Experiments with an MRI-Compatible Silicon Photomultiplier PET Scanner*, J. Nucl. Med. 53, 608–614, 2012.

[9] A. Kolb, H. F. Wehrl, M. Hofmann, et al., *Technical performance evaluation of a human brain PET/MRI system*, Eur. Radiol. 22, 1776–1788, 2012.

[10] Y. Lu, K. Yang, K. Zhou, et al., *Development of a SiPM-based PET imaging system for small animals*, Nucl. Instrum. Meth. A 743, 30–38, 2014.

[11] E. Roncali and S. R. Cherry, *Application of Silicon Photomultipliers to Positron Emission Tomography*, Annals of Biomedical Engineering, 39, 1358–1377, 2011.

[12] N. Giokaris, G. Loudos, D. Maintas, et al., *Partially slotted crystals for a high-resolution γ-camera based on a position sensitive photomultiplier*, Nucl. Instrum. Meth. A 550, 305–312, 2005.

[13] A.J. Gonzalez, S. Majewski, J. Proffitt, et al., *Continuous or pixelated scintillators?, not longer a discussion*, in 2014 IEEE Nuclear Science Symposium Conference Record, M19-114-1472.

[14] A. Gonzalez-Montoro, A. Aguilar, G. Cañizares, et al., *Performance Study of a Large Monolithic LYSO PET Detector With Accurate Photon DOI Using Retroreflector Layers*, Trans. Rad. Plasma Med. Scie. 1, 229, 2017.

[15] R. Pani, S. Nourbakhs, P. Pani, et al., *Continuous DOI determination by gaussian modelling of linear and non-linear scintillation light distributions*, IEEE NSS-MIC Conference Record, pp. 3386-3389, 2011.

[16] R. Pani, A.J. Gonzalez, M. Bettiol, et al., *Preliminary evaluation of a monolithic detector module for integrated PET/MRI scanner with high spatial resolution*, J. Instrum. 10, C06006, 2015.